The Astrophysical Journal, 644:484–496, 2006 June 10

RADIATIVE HYDRODYNAMIC MODELS OF OPTICAL AND ULTRAVIOLET EMISSION FROM M DWARF FLARES

Joel C. Allred,[1] Suzanne L. Hawley,[2] William P. Abbett,[3] and Mats Carlsson[4]
Received 2005 August 10; accepted 2006 February 9

ABSTRACT

We report on radiative hydrodynamic simulations of M dwarf stellar flares and compare the model predictions to observations of several flares. The flares were simulated by calculating the hydrodynamic response of a model M dwarf atmosphere to a beam of nonthermal electrons. Radiative back-warming through numerous soft X-ray, extreme-ultraviolet, and ultraviolet transitions are also included. The equations of radiative transfer and statistical equilibrium are treated in non-LTE for many transitions of hydrogen, helium, and the Ca II ion, allowing the calculation of detailed line profiles and continuum radiation. Two simulations were carried out, with electron beam fluxes corresponding to moderate and strong beam heating. In both cases we find that the dynamics can be naturally divided into two phases: an initial gentle phase in which hydrogen and helium radiate away much of the beam energy and an explosive phase characterized by large hydrodynamic waves. During the initial phase, lower chromospheric material is evaporated into higher regions of the atmosphere, causing many lines and continua to brighten dramatically. The He II 304 line is especially enhanced, becoming the brightest line in the flaring spectrum. The hydrogen Balmer lines also become much brighter and show very broad line widths, in agreement with observations. We compare our predicted Balmer decrements to decrements calculated for several flare observations and find the predictions to be in general agreement with the observations. During the explosive phase both condensation and evaporation waves are produced. The moderate flare simulation predicts a peak evaporation wave of $\sim$130 km s^{-1} and a condensation wave of $\sim$30 km s^{-1}. The velocity of the condensation wave matches velocities observed in several transition region lines. The optical continuum also greatly intensifies, reaching a peak increase of 130% (at 6000 Å) for the strong flare, but does not match observed white-light spectra.

Subject headings: hydrodynamics — radiative transfer — stars: atmospheres — stars: chromospheres — stars: flare — stars: low-mass, brown dwarfs

1. INTRODUCTION

Solar-type flares are common on cool stars with outer convective envelopes. Extensive observations of flares on magnetically active M dwarfs (dMe) in the solar neighborhood have revealed many similarities, including the presence of enhanced and broadened Balmer emission, increases in optical white-light and radio emission, and similar timescales for the impulsive and gradual phases. A detailed comparison of solar and stellar flares is presented in Haisch et al. (1991). The generally accepted model of solar flares assumes that reconnecting magnetic fields cause the acceleration of electrons (and possibly protons). The accelerated electrons travel down magnetic field lines, impacting in the lower atmosphere, producing hard X-ray bremsstrahlung, and causing increased optical continuum and line emission. As the electrons heat the lower atmosphere, it expands and "evaporates" into the transition region and corona, thereby increasing the thermal soft X-ray flux. The Neupert effect describes the relationship between hard and soft X-rays on the Sun (Neupert 1968; McTiernan et al. 1999), and stellar observations of the Neupert effect (Hawley et al. 1995, 2003 [hereafter H03]; Guedel et al. 1996; Mitra-Kraev et al. 2005) provide evidence that stellar and solar flare processes show similar effects.

Even though solar and stellar flares are likely to be produced by the same basic mechanisms, the different physical conditions on M dwarfs compared to the Sun give rise to a number of observational differences. Flares on dMe stars occur more frequently and are often much more energetic than solar flares. This is likely the result of the stronger magnetic fields on dMe stars (Johns-Krull & Valenti 1996), which produce more magnetic activity than on the Sun. For stellar flares, increases in the optical continuum are very common; this is often taken as the defining observational signature of a flaring star. However, detectable elevations in the optical continuum are rare in solar flares, since the Sun has much brighter background continuum emission, and therefore only the largest flares produce enough white-light contrast to be seen.

On the Sun, impulsive hard X-rays are spatially and temporally correlated with increased white-light emission (Hudson et al. 1992). By extension, the rapid rise in near-ultraviolet and blue emission seen in stellar flares is thought to correspond with the solar impulsive phase. Therefore, stellar optical flares are likely to be the analog to solar white-light flares. We recently developed models of impulsive solar white-light flares (Allred et al. 2005, hereafter A05), and in this paper we apply those techniques to model impulsive M dwarf flares. Previous and recent M dwarf flare observations (Rodono et al. 1984; Doyle et al. 1988; Phillips et al. 1988; Hawley & Pettersen 1991; Eason et al. 1992; Abdul-Aziz et al. 1995; Jevremovic et al. 1998; H03) are used to provide observational constraints on the models.

The paper is organized as follows. In § 2, we briefly outline the method by which the radiative hydrodynamic (RHD) equations are solved. We also describe the procedure used to generate the initial atmosphere and the methods for incorporating soft X-ray

[1] Department of Physics, University of Washington, Box 351560, Seattle, WA 98195.
[2] Department of Astronomy, University of Washington, Box 351580, Seattle, WA 98195.
[3] Space Sciences Laboratory, University of California, Berkeley, CA, 94720.
[4] Institute of Theoretical Astrophysics, University of Oslo, P.O. Box 1029, Blindern, N-0315 Oslo, Norway.

and electron beam heating into the simulations. In § 3, we discuss the dynamics of our simulations and present detailed line and continuum profiles. In § 4, we compare the M dwarf models to the solar models of A05, while in § 5 we compare predictions of our models to stellar flare observations. In § 6 we present our conclusions.

2. METHOD OF SOLUTION

The method we have used is described in detail in A05 and Abbett & Hawley (1999, hereafter AH99), and we refer the reader to those papers for a more detailed discussion. The equations of hydrodynamics, statistical equilibrium, and radiative transfer are solved on a one-dimensional adaptive grid using the RADYN code (Carlsson & Stein 1994, 1995, 1997).

The preflare atmosphere was generated in a manner similar to AH99. We assume that the plasma moves along field lines in a flux tube, which we approximate as a one-dimensional cylinder. Our model flux tube extends from the photosphere to the corona and has a length of 10^9 cm. The preflare atmosphere of Hawley & Fisher (1992) was used as the initial starting state for the atmospheric structure. Constant nonradiative quiescent heating was applied to grid zones with photospheric column mass (i.e., column mass greater than 3.16 g cm^{-2}) to balance the energy losses in the photosphere. The upper boundary was held at 6×10^6 K. With these boundary conditions and no external sources of heating, the atmosphere was allowed to relax to a state of hydrostatic equilibrium.

We modeled a flare by calculating the RHD response to a beam of nonthermal electrons injected at the top of the loop. The electron beam heats the stellar atmosphere, which increases the soft X-ray, extreme-ultraviolet, and ultraviolet radiation (hereafter, we refer to these collectively as XEUV flux); this further heats the atmosphere through radiative back-warming. For the dynamic simulations, we change the upper boundary condition to a transmitting boundary and remove its temperature constraint. We note that with no external source of coronal heating our coronal model will cool. However, the timescale for coronal cooling is much greater than the impulsive timescale (Cargill 1994). As the flare evolves, material flows through the upper boundary, emulating the expansion of the flux tube. Since our flux tube has a fixed length of 10^9 cm, the loop apex and the upper corona move outside the region of computation during the course of the flare simulation. Our concern in this paper is modeling optical and UV emission, which primarily originate from the lower atmosphere. In A05, we found that chromospheric heating from the upper corona was negligible when compared to the energy deposited by the electron beam. Thus, the "loss" of the upper corona is not likely to affect the chromospheric emission.

The non-LTE atomic level populations are obtained for a six-level hydrogen atom with continuum, a nine-level helium atom with continuum, and a six-level Ca II ion with continuum using the technique of Scharmer & Carlsson (1985). We calculate numerous bound-bound and bound-free transitions in detail. These are listed in Tables 1 and 2 of A05. Complete redistribution is assumed for all transitions, but the effects of partial redistribution are approximated for the Lyman transitions by truncating the line profiles at 10 Doppler widths. Other transitions are included as background opacity in LTE. The opacities were obtained from the Uppsala package of Gustafsson (1973). We include optically thin radiative cooling from bremsstrahlung and coronal metal transitions using emissivities acquired from the ATOMDB database (Smith et al. 2001). The equations are solved on an adaptive grid using 250 grid points in depth, 5 in angle, and up to 100 in frequency for each transition.

Numerous observations of hard X-rays during *solar* flares indicate the presence of downward-directed nonthermal electrons impacting in the lower solar atmosphere. Unfortunately, current instruments are unable to detect hard X-rays produced from flares on stars other than the Sun. However, as mentioned above, observations of the Neupert effect provide justification that the heating mechanisms may be the same. Therefore, in these models we employ an electron beam as the source of heating in the lower stellar atmosphere. In particular, we use an electron beam with energy spectrum obtained by Holman et al. (2003) for the 23 July 2002 X-class *solar* flare observed by RHESSI. The injected electrons are found to have a double power-law energy distribution of the form

$$F_0(E_0) = \begin{cases} \dfrac{\mathcal{F}(\delta_{\mathcal{U}} - 2)(\delta_{\mathcal{L}} - 2)}{E_c^2\left[(\delta_u - 2) - (E_B/E_c)^{2-\delta_l}(\delta_u - \delta_l)\right]} \left(\dfrac{E_0}{E_c}\right)^{-\delta_l} \\ \quad \text{for } E_0 < E_B, \\ \dfrac{\mathcal{F}(\delta_{\mathcal{U}} - 2)(\delta_{\mathcal{L}} - 2)}{E_c^2\left[(\delta_u - 2) - (E_B/E_c)^{2-\delta_l}(\delta_u - \delta_l)\right]} \left(\dfrac{E_B}{E_c}\right)^{\delta_u - \delta_l} \\ \quad \text{for } E_0 > E_B, \end{cases} \tag{1}$$

where $\mathcal{F}$ is the electron energy flux that enters the magnetic loop, E_c is the cutoff energy below which the X-ray emission is assumed to be thermal, and E_B is the break energy, where the distribution shifts from spectral index δ_l to δ_u. We take δ_l, δ_u, E_c, and E_B to be constant, with values of 3.0, 4.0, 37 keV, and 105 keV, respectively, corresponding to the peak of the 23 July 2002 flare. The rate of energy deposited by the electron beam is modeled using the technique of Emslie (1978).

During flares, the density in the transition region and corona becomes elevated, increasing the number of XEUV photons originating from these regions. The outward-directed photons we detect as enhanced emission, while the downward-directed photons heat the lower atmosphere through increased photoionizations. We have used the ATOMDB database to determine the thermal volume monochromatic emissivity as a function of wavelength and temperature. We include line emissivities calculated for approximately 34,000 transitions at 37 temperature points ranging from 10^4 to 10^7 K. We have grouped the transitions into 14 wavelength bins with a range of 1–2500 Å. Table 3 in A05 lists the range and emissivity-weighted central wavelengths of each bin. The XEUV back-warming rate is calculated from equation (6) of A05 with the assumption that the energy from the photoionized electrons is entirely converted to heat.

3. FLARE SIMULATIONS

We carried out two flare simulations, corresponding to moderate beam heating with an electron flux of $\mathcal{F} = 10^{10}$ ergs cm^{-2} s^{-1} (the F10 flare) and strong beam heating with $\mathcal{F} = 10^{11}$ ergs cm^{-2} s^{-1} (the F11 flare). The F10 flare was evolved for 230 s and the F11 flare for 15 s. In both cases the beam energy spectrum is given by the double power law as described in equation (1).

3.1. *F10 Flare Dynamics*

Figure 1 shows the evolution of the temperature and density stratification, the electron beam energy deposition rate, the ionization fraction, and the electron density during the F10 flare. The electron beam initially penetrates to a depth of 0.26 Mm, and

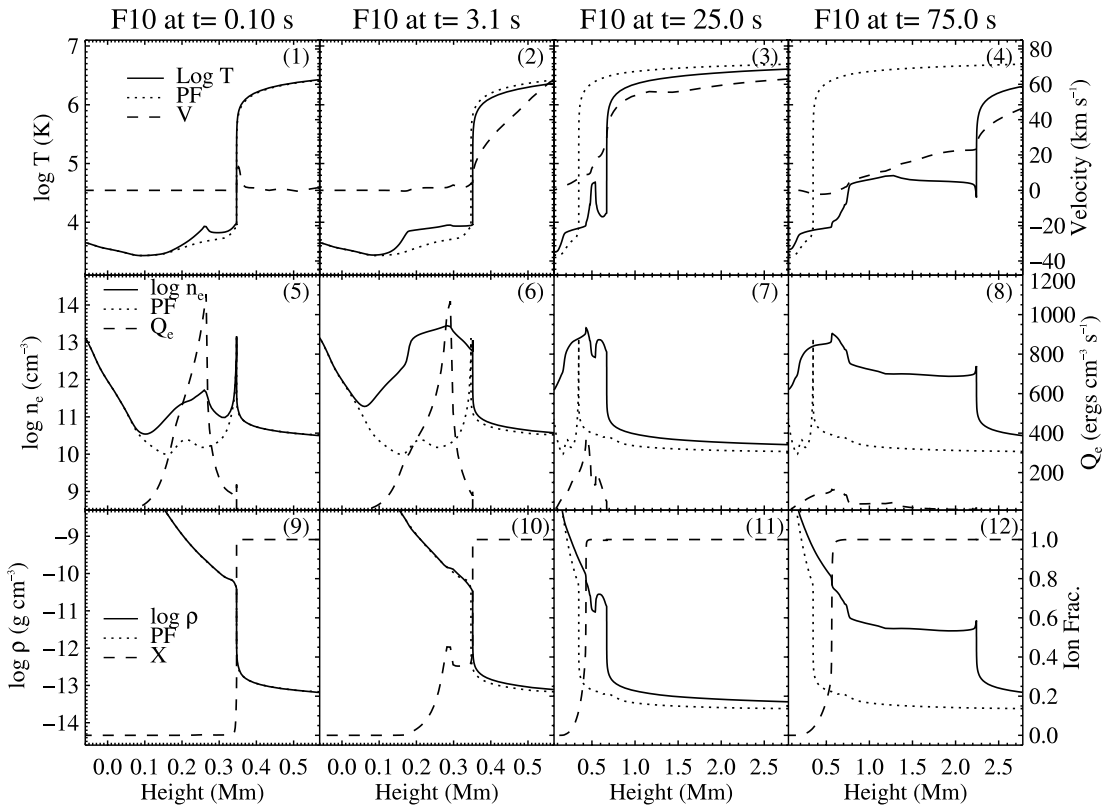

FIG. 1.—Stellar atmosphere at four times during the initial phase of the F10 flare. The top row shows the log of the temperature, T (*left axis*), and velocity (*right axis*) as a function of height compared with the preflare state (PF). In the middle row the electron density, n_e (*left axis*), and beam heating rate, Q_e (*right axis*), are plotted. The bottom row shows the mass density, ρ (*left axis*), and hydrogen ionization fraction, X (*right axis*). Note the change in scale of the horizontal axis in the third and fourth columns.

the surrounding temperature quickly rises in response (the first column of Fig. 1). A large hydrodynamic wave forms and begins to carry material from the chromosphere into the transition region. By 0.25 s, the temperature plateaus at ~9000 K in the region of beam energy deposition as a result of elevated hydrogen radiative cooling. For the next several seconds, the flare evolves slowly as much of the beam energy is radiated away by hydrogen emission (the second column of Fig. 1). This results in significantly stronger hydrogen emission lines. The transition region continues to fill up with plasma evaporated from the chromosphere and becomes extended in height (see panels 3 and 4 of Fig. 1). By 10.0 s most of the hydrogen in the region of beam heating is ionized, and the radiative cooling is no longer able to balance the beam heating. The atmosphere rapidly heats to a temperature of ~50,000 K, but by 25.0 s it again plateaus (third column of Fig. 1). This time the equilibrium is a result of helium radiative cooling, and a relatively gentle phase begins as hydrogen and helium radiate away most of the beam energy. We note that although the plasma in the extended transition region ($z = 0.8$–2.2 Mm in panel 4 of Fig. 1) appears to have "cooled" when compared to the preflare atmosphere, this is not the case. Material from lower, cooler regions is brought upward and heated. For example, the plasma located in this region has a temperature of about 60,000 K at 75.0 s, but originates in the chromosphere from a height of 0.3 Mm and a temperature of 5000 K. In general, when comparing the atmospheric structure during the flare evolution, care must be taken to consider that the plasma has moved.

By 98 s, the helium in the region of beam heating has become almost completely ionized and can no longer effectively cool the atmosphere (panel 9 of Fig. 2). The atmosphere responds by explosively heating. The temperature quickly rises (panel 2 of Fig. 2), and a large hydrodynamic wave is created. We refer to this period as the explosive phase. Explosive phase dynamics are shown in Figure 2. A high-temperature bubble forms in the region near 1.5 Mm (second column of Fig. 2), and for the next 130 s the bubble expands as the wave propagates through the atmosphere. This stellar flare simulation was not able to track the wave passing through the top of flux tube and did not attain a steady state. Our final atmosphere (last column of Fig. 2) has a denser corona and transition region (panel 8) than the preflare atmosphere. We note that much of the original corona has flowed through the original flux tube boundary. In A05 we found for solar flare simulations that after the wave passed through the boundary of the flux tube the loop heated quickly. The solar flare loop top eventually reached a steady state temperature approximately 5 times the preflare value, and we expect a similar result for stellar flare loops.

The gentle and explosive phase energetics are plotted in Figure 3. During the gentle phase, the energy deposited by the beam is essentially balanced by radiative cooling (panel 1). A small amount of energy goes into increasing the helium ionization in the region 1.0–1.5 Mm (see the inset in panel 2). Once the helium is completely ionized, the radiative cooling sharply drops, and the explosive phase begins. In the explosive phase, there is a significant portion of the beam energy in the region of the expanding high-temperature bubble (see panel 2 of Fig. 2) that is not radiated away (panel 3 of Fig. 3). Most of this energy goes into increasing the temperature (panel 4) and expanding the bubble [see $Pd(1/\rho)$ in panel 3].

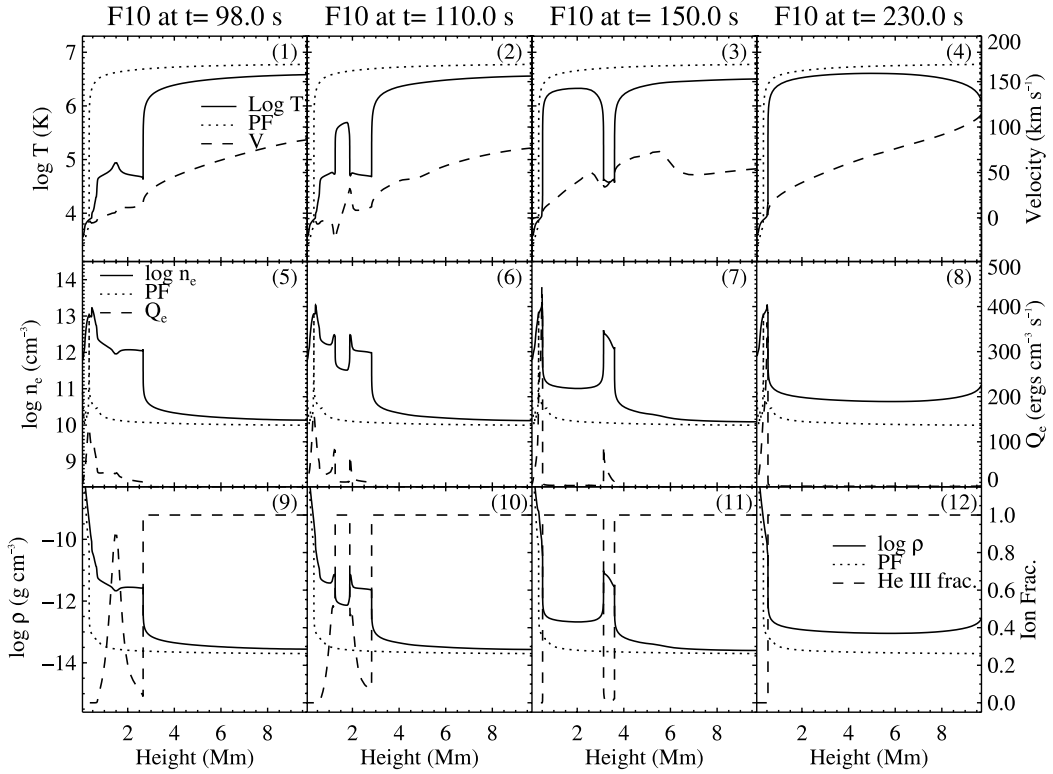

FIG. 2.—F10 flare atmosphere at four times during the explosive phase. The quantities plotted are identical to Fig. 1, except that the He III fraction, rather than the hydrogen ionization fraction, is plotted in the bottom row.

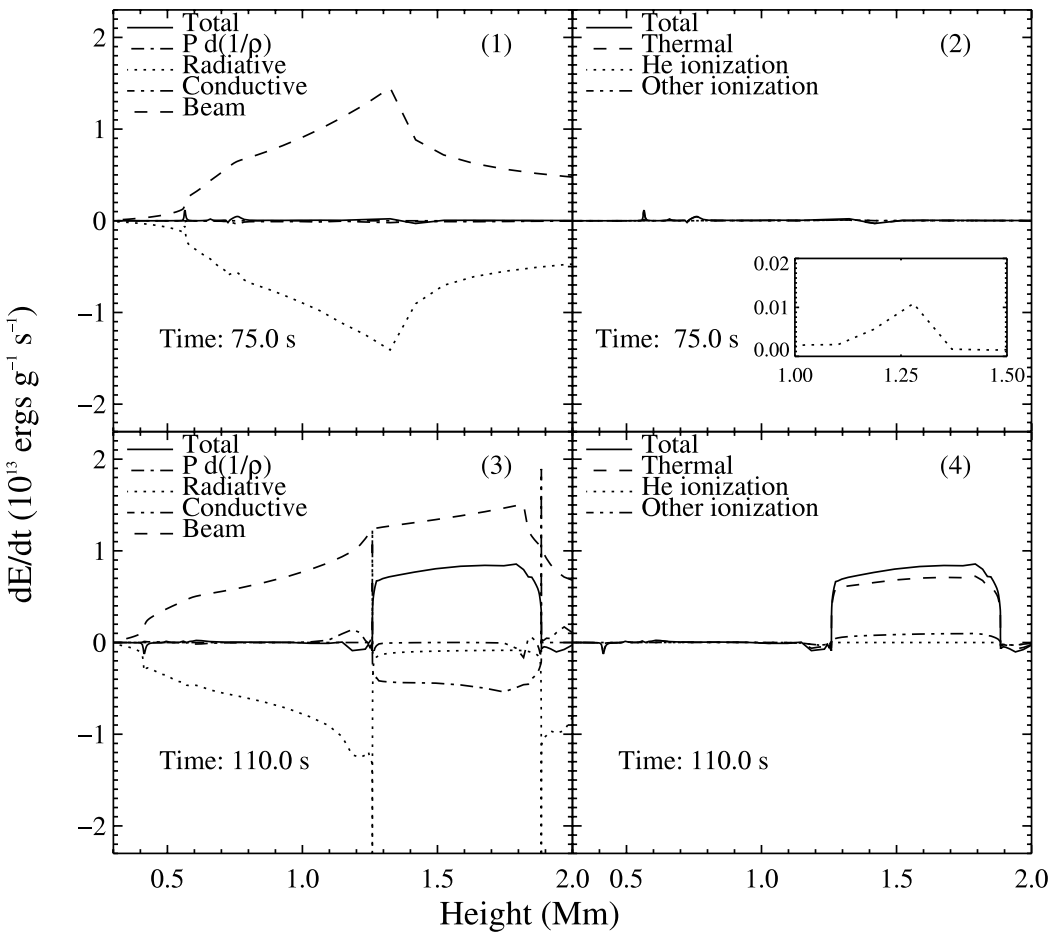

FIG. 3.—Energetics for the F10 flare during the gentle phase (panels 1 and 2) and the explosive phase (panels 3 and 4). The atmospheric structure for panels 1 and 2 is shown in the last column of Fig. 1, and the structure for panels 3 and 4 is shown in the second column of Fig. 2. Important terms in the energy conservation equation are shown in panels 1 and 3, and contributions to the change in internal energy are shown in panels 2 and 4. The inset in panel 2 shows a close-up view of the rise in internal energy due to increased He ionization.

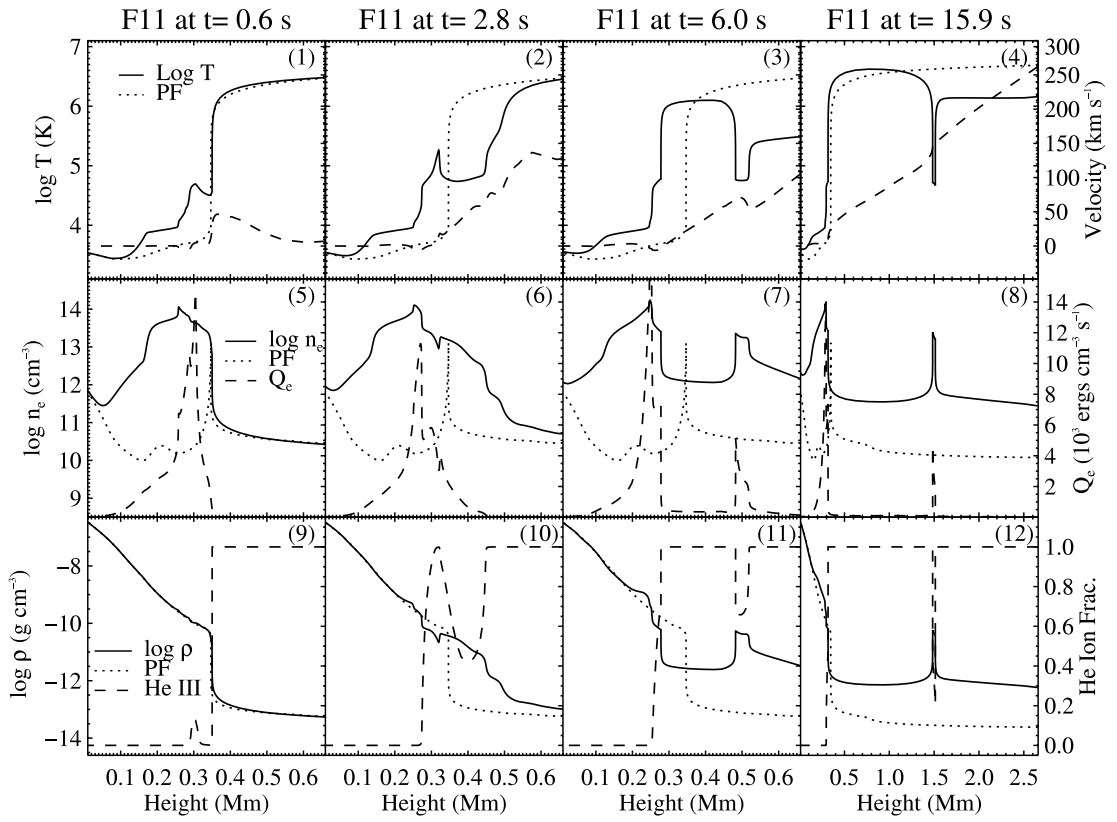

FIG. 4.—Flare atmosphere at four times during F11. The quantities plotted are identical to Fig. 1, except that the He III fraction, rather than the hydrogen ionization fraction, is plotted in the bottom row.

3.2. *F11 Flare Dynamics*

The evolution of the F11 flare is similar to F10, but proceeds much faster. Figure 4 shows the atmosphere at several times during this flare. As in F10, the beam initially penetrates to a height of 0.26 Mm, and in response the atmosphere rapidly heats to about 10,000 K. A strong hydrodynamic wave begins to carry material into the transition region. By 0.03 s, the temperature increase has stabilized, as the beam heating is in equilibrium with hydrogen radiative cooling. This equilibrium lasts until 0.16 s, when most of the hydrogen in the region of beam heating has been ionized. In a fashion similar to F10, the atmosphere again quickly heats, but by 0.5 s plateaus at 50,000 K as a result of an equilibrium of beam heating with helium radiative cooling (first column of Fig. 4). By 2.5 s, helium in the region of 0.3 Mm is completely ionized, and the atmosphere undergoes explosive heating (second column of Fig. 4). As in F10, a high-temperature bubble forms and propagates toward the boundary of the flux tube. A notable difference between F10 and F11 is the height at which this happens, $\sim$2 Mm in F10 compared to 0.3 Mm in F11; see panel 2 of Figure 2 and panel 2 of Figure 4. The evolution of F11 is much quicker than F10, so less material has had time to evaporate into the upper atmosphere. The beam therefore deposits most of its energy lower in the atmosphere in F11 than in F10. At 15.9 s there is a very steep decrease in temperature at $z = 1.5$ Mm (panel 4). This is caused by the high level of radiative cooling due to increased density at the front of the outward-directed explosive wave. This is likely an artifact of the simulation, as strongly blueshifted transition region material is not seen in flare observations (see § 5.6).

3.3. *Line Profiles*

Mass motions during the flare simulations cause significant Doppler shifts and introduce large asymmetries in the line profiles. Figure 5 shows line profiles for four important lines during F10. The first column (panels 1, 6, 11, and 16) shows that at 1.0 s these emission lines have increased in intensity, but there are no large mass motions, since the line profiles are relatively symmetric. In the second column, however, the line profiles are significantly distorted as a result of large velocities produced by flare heating. The line profiles are especially complicated when they are formed in regions of oppositely directed waves. For example, the Hα profile in panel 2 has an enhanced red wing, indicating downward-directed plasma, but its line center is blueshifted. The line center is formed higher in the stellar atmosphere than the wings, where the plasma is "evaporating" into the transition region. In panel 5, Hα has a very large blue wing. This is the result of the high-velocity, high-density evaporation wave passing through the boundary of the flux tube. Hβ responds to flare heating very quickly. By 1.0 s (panel 6), it is already about 150 times brighter than in the preflare atmosphere. Also note that Hβ becomes very broad, as discussed in more detail in § 5.3. The He II 304 line becomes very bright as a result of the extended transition region that forms during the gentle phase (see panel 4 of Fig. 1). During this phase, it becomes the most intense line in the flaring spectrum. The He II 304 flux reaches a maximum at the onset of the explosive phase (Fig. 5, panel 13). Once the explosive phase begins, the atmosphere heats beyond 50,000 K (i.e., the temperature of formation of He II) and the intensity decreases (panels 14 and 15). In panel 14, a 22 km s^{-1} wave

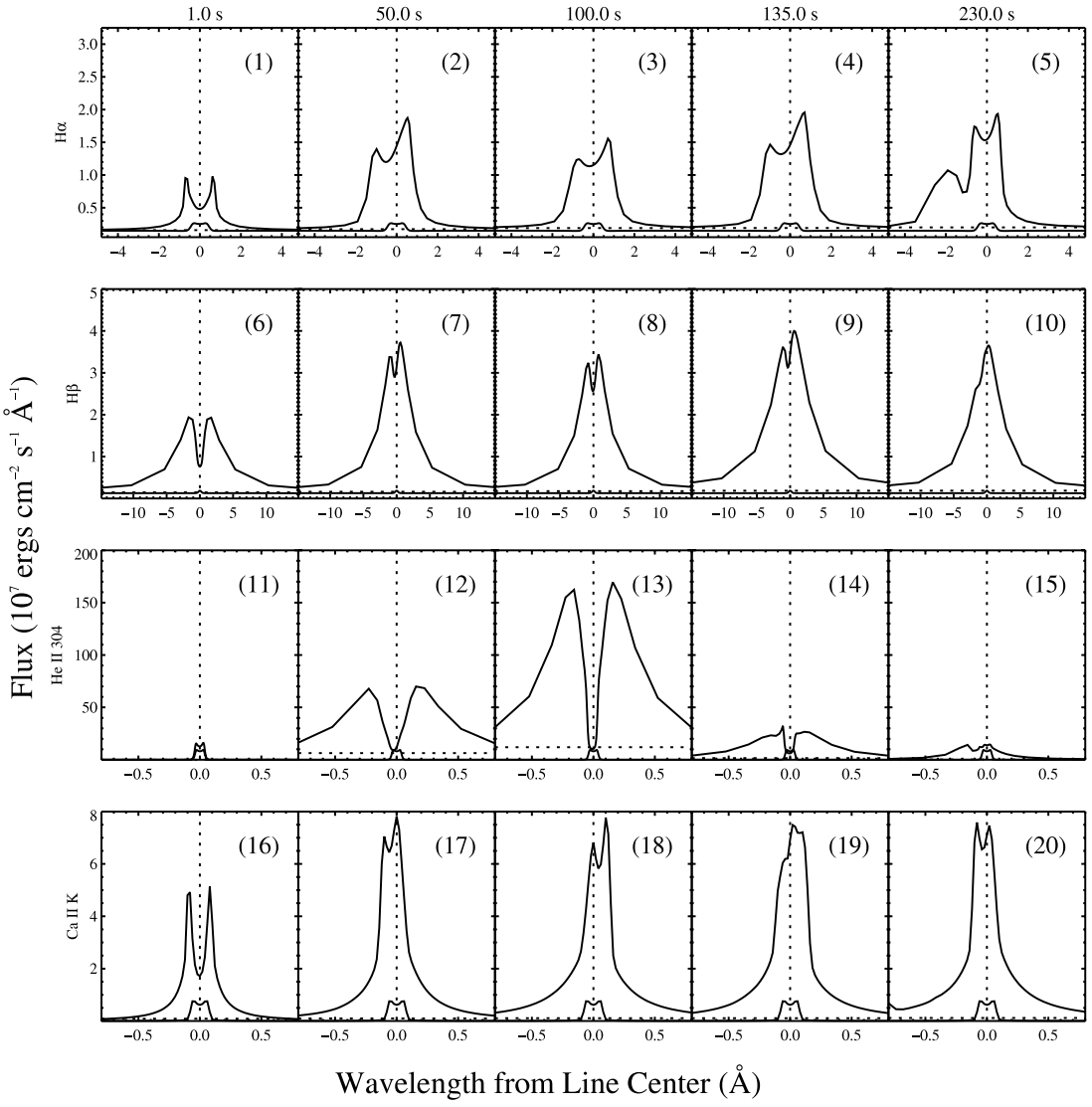

FIG. 5.—Line profiles plotted for Hα, Hβ, He II 304, and Ca II K at five times during F10. The smaller line profile in each panel is the quiescent line profile. The horizontal dotted line indicates the flare continuum level, and the vertical dotted line is line center.

produced at the onset of the explosive phase causes an enhanced blue peak in the He II 304 line profile. As this wave passes into the higher temperature regions of the corona, it begins to move faster. By 230 s, the wave is moving at 129 km s^{-1}, and He II 304 shows a strong blueshift (panel 15). In contrast, the Ca II K line is sensitive to velocities in the chromosphere. In panel 17, Ca II K is blueshifted, indicating evaporation of chromospheric material into the transition region. The Ca II K line profiles in panels 18 and 19 are redshifted as a result of chromospheric condensation waves. At 100 s, a relatively slow ($\sim$6 km s^{-1}) downward-directed wave produced from the initial beam impact passes through the region of Ca II K formation, producing the redshift (panel 18). At 135 s, a much faster condensation wave ($\sim$30 km s^{-1}), produced from the explosive increase in temperature, passes through this region, and Ca II K is further redshifted (panel 19).

3.4. *Continuum*

Our flare simulations exhibit strongly enhanced optical continuum emission. Figure 6 shows optical continuum spectra for the preflare atmosphere and a few times during the F10 (Fig. 6*a*) and F11 (Fig. 6*b*) flares. A large Balmer jump and noticeable Paschen jump are clearly present in these spectra. The elevated flux peaking at about 6500 Å is primarily the result of blackbody emission and indicates heating has occurred in the photosphere. The electron beam is unable to penetrate deeply enough to directly heat the photosphere; instead, the heating in this region is primarily due to radiative back-warming from the Balmer and Paschen continua. This is shown in Figure 7, which plots the energy deposited in the lower atmosphere as a function of height above the photosphere. Important contributors to the gain in internal energy are plotted in Figure 7*a*, showing that energy deposited by radiation is the dominant form of flare heating in the photosphere. Figure 7*b* plots the most important contributors to the radiative heating and indicates that Balmer and Paschen continua significantly heat the lower atmosphere. The photosphere reaches a maximum temperature increase of 400 K for F10 and 1200 K for F11. This, together with the elevated Paschen continuum, produces a 32% and a 129% increase in the optical continuum (measured at 6000 Å) for F10 and F11, respectively.

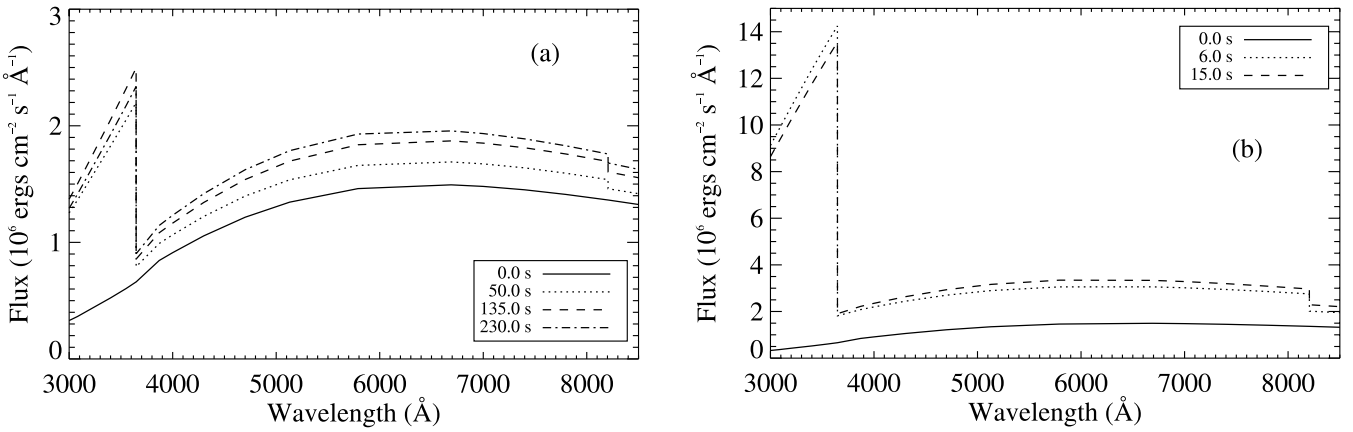

FIG. 6.—Continuum spectra plotted for the preflare atmosphere and a few times during (*a*) the F10 and (*b*) the F11 flares. The spectra exhibit a large Balmer jump (3646 Å), a noticeable Paschen jump (8205 Å), and increased blackbody emission.

4. COMPARISONS TO THE SOLAR FLARE MODELS OF A05

Compared to the Sun, an active M dwarf has a higher surface gravity, a cooler photosphere, and a hotter corona. Figure 8*a* compares the temperature structure of our M dwarf preflare atmosphere with the solar preflare atmosphere used in A05. The higher surface gravity on the M dwarf compresses the atmosphere relative to the Sun, causing the chromosphere and transition region to be closer in height to the photosphere than in the solar model. The density of the M dwarf corona is approximately an order of magnitude greater than the solar corona. The compressed atmosphere results in a much narrower range of beam energy deposition (shown in Fig. 8*b*).

Many of the features predicted by the solar models of A05 are similar to those in the M dwarf simulations presented here. For example, despite differences in atmospheric structure, both types of simulations predict chromospheric evaporation waves of similar speeds. The reason for this is that the beam energy is deposited in each atmosphere at nearly the same column mass. Since the same beam energy is assumed in the solar F10 and M dwarf F10 simulations and the mass above the beam impact location is nearly the same, similar velocities should be expected. Another important similarity is that both types of simulations exhibit an initial gentle phase followed by explosive eruption in the transition region when the balance between flare heating and radiative cooling is broken. However, there is significant difference between the M dwarf and solar models in the onset time of the explosive phase. The explosive phase starts at 98 and 2.5 s for the M dwarf F10 and F11 flares, respectively, and at 73 and 1.0 s for the solar F10 and F11 flares, respectively. The reason for this is that since the M dwarf model has a higher coronal density, it takes longer for the helium to be fully ionized, so that the beam heating overcomes the radiative cooling.

Another difference is the intensity of the emitted radiation. In the solar model, the helium-emitting plateau in the transition region becomes much more extended than in the M dwarf models (compare the first panels of Fig. 2 and Fig. 4 of A05), causing a larger He II 304 enhancement in the solar case. This is seen in Figure 9, which shows light curves for the He II 304 line during the F10 solar and M dwarf simulations. In both cases, the He II 304 flux peaks at the onset of the explosive phase. In contrast, the hydrogen Balmer line emission is stronger in the M dwarf flare spectrum. Since the Sun has a hotter photosphere, the continuum level is much higher for the solar Balmer lines. The Balmer line profiles for the solar and M dwarf cases are

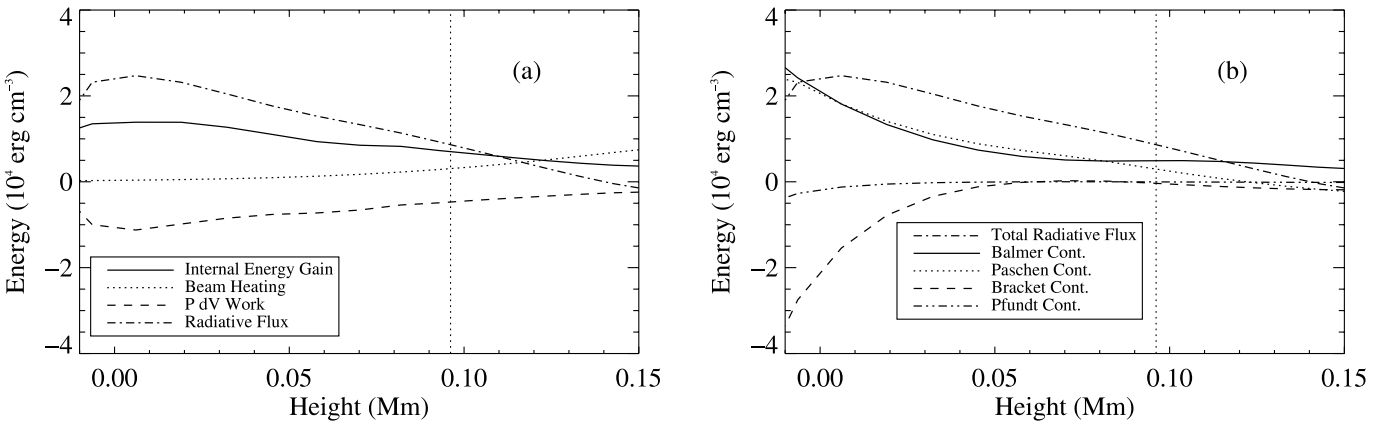

FIG. 7.—Internal energy gain in the lower atmosphere as a function of height above the photosphere. (*a*) The solid line represents the total internal energy gain. The dotted line is the energy deposited by the beam. The dashed line is the *PdV* work, and the dot-dashed line is the radiative flux. The heating from radiation dominates in the photosphere. (*b*) Contributions to the total radiative flux. The Balmer, Paschen, Bracket, and Pfundt continua are represented by the solid, dotted, dashed, and dot-dot-dot-dashed lines, respectively. The Balmer and Paschen continua are the dominant sources of heating in this region. Lyman continuum does not significantly contribute to the energetics this low in the atmosphere and is not included in the plot.

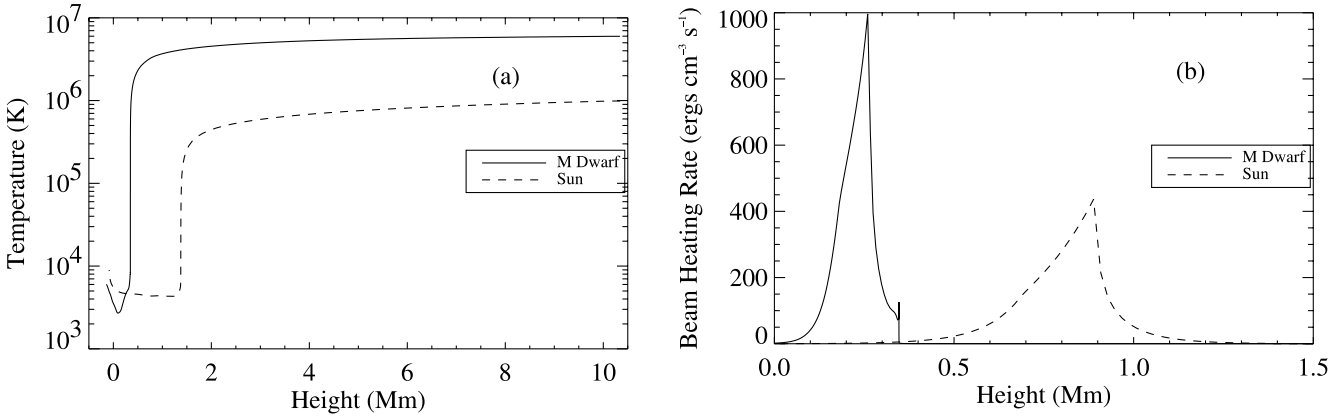

FIG. 8.—(*a*) Temperature structure of the preflare M dwarf (*solid line*) and solar (*dashed line*) atmospheres. (*b*) Initial beam energy deposition rate for the M dwarf (*solid line*) and solar (*dashed line*) cases.

similar, but since the line-to-continuum ratio is higher in the M dwarf case, it has more Balmer line emission. The Hβ line profile in Figure 10 illustrates this effect.

5. COMPARISON TO M DWARF FLARE OBSERVATIONS

5.1. *Continuum*

Numerous photometric observations of flares on active M dwarfs have shown that the continuum spectrum fits well to a blackbody of approximately 9000 K (Hawley & Fisher 1992; Eason et al. 1992; Alekseev et al. 1994; H03). This is puzzling because the electron beam, which is the assumed source of flare heating, is unable to deposit sufficient energy in the photosphere to heat it to so high a temperature. One explanation, proposed by Hawley & Fisher (1992), suggested that XEUV back-warming may be responsible for heating the photosphere during flares. To test this, we included XEUV back-warming as described in § 2. Figure 11 plots the energy deposited during the F10 flare due to XEUV emission and compares it to beam heating. We find that the XEUV heating is about a hundred times smaller than the beam heating and does not significantly contribute to heating the photosphere. As discussed in § 3.4, Balmer and Paschen continuum back-warming does heat the photosphere, but even this is insufficient to raise the temperature to 9000 K.

Another explanation is that the observed *UBVR* enhanced spectrum may not actually be the result of blackbody emission, but rather may be due to increased Balmer emission from the chromosphere. This explanation is supported by these simulations. Despite a lack of direct photospheric heating, when convolved with the *UBVR* bandpasses these simulations do produce a spectrum with the general shape of a blackbody with a temperature of 8000–9000 K. Figure 12 shows an example of the convolved spectrum and blackbody fit. In a fashion similar to H03 we include an additional measurement in the UV, centered at 1469 Å. The spectrum is similar to observed continuum enhancements seen during flares (cf. Fig. 10 of H03), and therefore, it is plausible that the ubiquitous white-light continuum may not be thermal in nature, but actually a result of Balmer and Paschen emission. However, the increased *U* band seen in our simulations is the result of a strongly elevated Balmer jump, which has not been observed in stellar flare spectra (Hawley & Pettersen 1991; Eason et al. 1992).

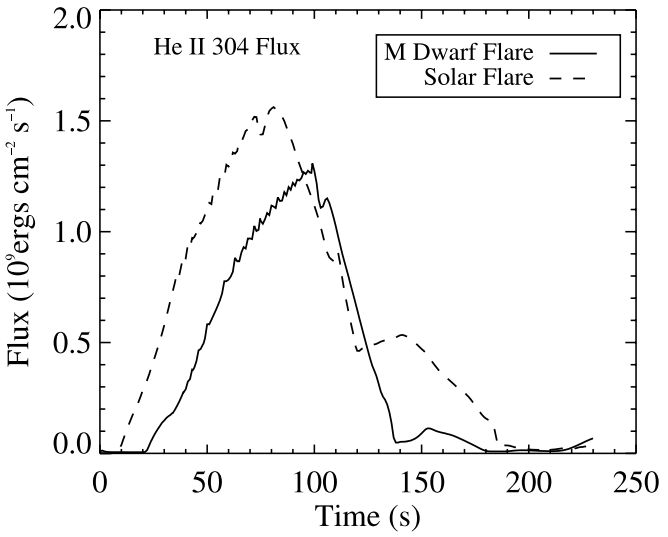

FIG. 9.—Light curves of the He II 304 line plotted for the F10 M dwarf simulation presented in this paper and the F10 solar model of A05. The explosive phase begins earlier, and there is more total emission in the solar case.

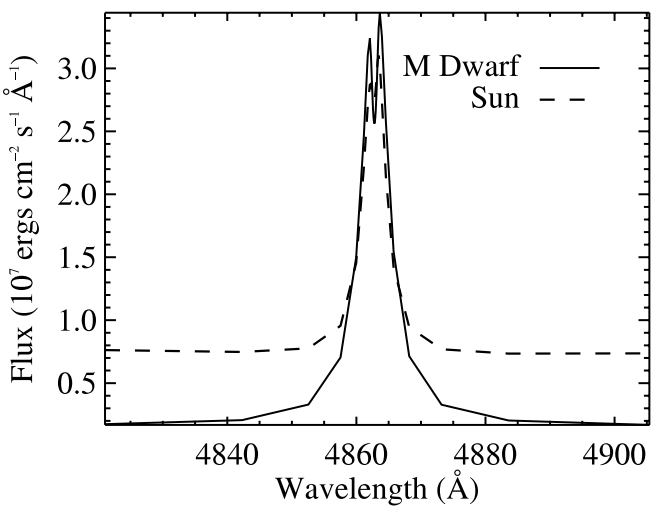

FIG. 10.—Hβ line profiles at 100 s for the F10 M dwarf simulation and the F10 model of A05. The line profiles are similar in shape and maximum intensity, but since the level of the continuum is higher in the solar case there is less total line emission.

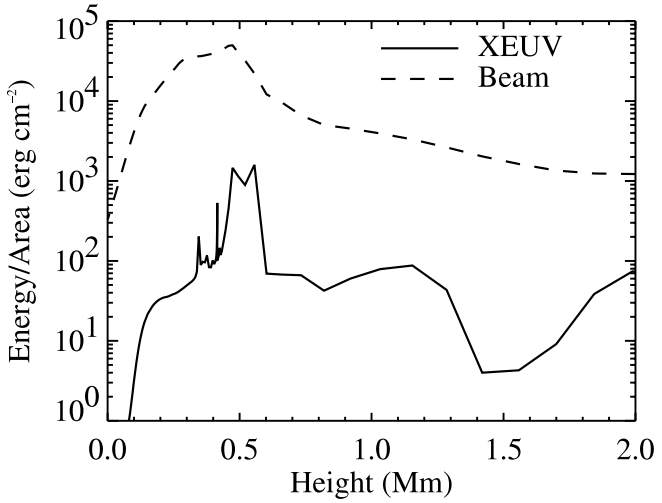

FIG. 11.—Energy deposited during the F10 flare through XEUV backwarming and electron beam heating plotted as a function of atmospheric depth. The XEUV heating accounts for about 1% of the total energy deposited.

5.2. *Continuum Dimming*

An initial dimming in the stellar continuum at the onset of a white-light flare has been observed by many authors (Cristaldi et al. 1980; Giampapa et al. 1982; Doyle et al. 1988; Hawley et al. 1995). In a manner similar to AH99 and A05, our simulations also exhibit initial continuum dimming. Figure 13 shows light curves for Balmer and higher order hydrogen continua. The continuum dimming seen here is a result of nonthermal ionization produced by the electron beam and can be understood as follows. The beam raises collisional rates in the upper chromosphere, causing higher population densities for the excited states of hydrogen. This increases the absorption probability for Balmer and higher order hydrogen continuum photons, which previously would have escaped and been seen as continuum emission. This results in an initial decrease in the continuum intensity. The time between flare onset and the rebrightening of the continuum is controlled by the ratio of recombinations to photoionizations. As the flare evolves, the increased electron density in the upper chromosphere elevates the recombination rate and begins to reduce the population excess of the excited states of hydrogen. This decreases the photoionization rate, and the continuum rebrightens.

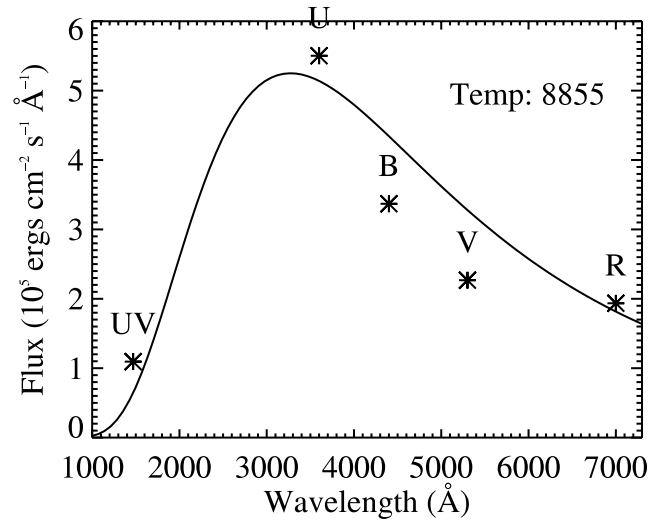

FIG. 12.—Flare spectrum convolved with the *UBVR* filters and the corresponding blackbody fit. The *UV* point is obtained by averaging the spectrum over three 30 Å regions centered at 1469 Å. The spectrum is best fit with a temperature of 8855 K.

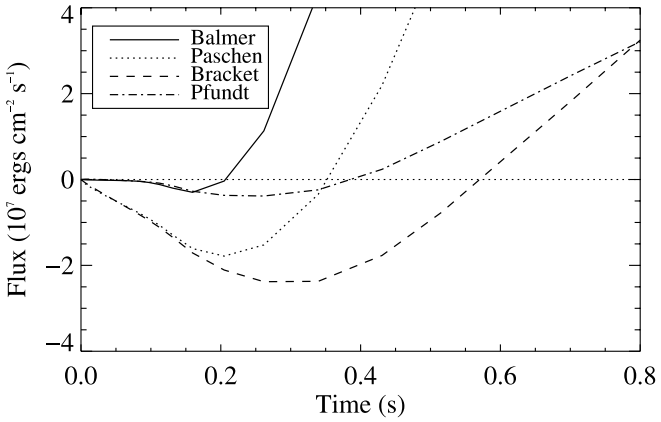

FIG. 13.—Fluxes for the Balmer, Paschen, Bracket, and Pfundt continua plotted as a function of time. This plot illustrates the initial continuum dimming seen in the higher order hydrogen continua.

5.3. *Line Broadening*

During the impulsive phase the Balmer lines dramatically increase in width, as observed by numerous authors (see, for example, Doyle et al. 1988; Phillips et al. 1988; Hawley & Pettersen 1991; Eason et al. 1992; Abdul-Aziz et al. 1995; H03). Figure 14 shows line profiles computed during F10 for Hβ and Hγ and compares them to line profiles observed during the impulsive peak of flare 8 of H03. Similarly, Figure 15 shows the Hγ line compared to the line profile obtained by Hawley & Pettersen (1991). In each case the quiescent line emission has been removed from the line profile. To aid in measuring the line width, smoothing

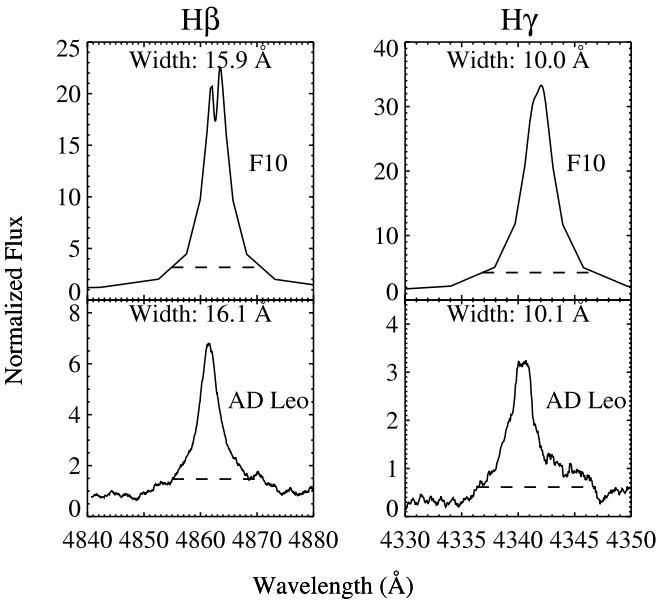

FIG. 14.—Normalized line profiles for Hβ and Hγ obtained from the F10 simulation compared with observed line profiles at the peak of flare 8 in H03. The line widths at 0.1 maximum are indicated by the dashed lines. The top row shows synthetic profiles from F10 at a characteristic time during the initial phase (64 s). The plots in the bottom row show flare spectra (quiescent emission has been removed) obtained from the peak of flare 8 from H03.

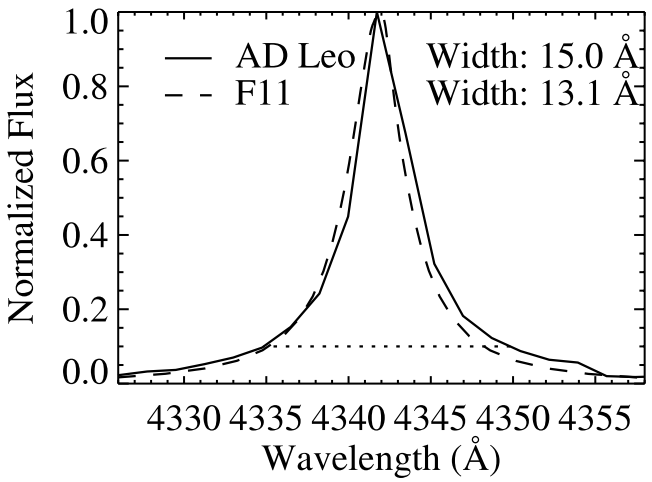

FIG. 15.—F11 Hγ line profile compared to the Hawley & Pettersen (1991) AD Leo flare observation. The simulated line profile is taken at the time of peak Hγ emission, and the observed line profile is taken at the peak of the flare (542 s). In each case, the continuum emission has been removed, and the line profile has been normalized to the line maximum. The Hawley & Pettersen (1991) line width at 0.1 maximum is indicated by the dotted line.

has been applied to the H03 observed line profile. To include the broadened wings, we measure line widths at 1/10 of maximum. In both the simulation and the H03 flare observation, Hβ increases to a width of about 16 Å, and Hγ reaches a peak line width of 10 Å. The Hawley & Pettersen (1991) flare was much larger than the H03 flare, and in this flare Hγ had a peak width of 15 Å compared to 13.1 Å obtained in our F11 simulation.

The observed line broadening is likely caused by either Stark broadening from the increased electron density in the flaring atmosphere or turbulent and mass motion flows in the flaring atmosphere. Doyle et al. (1988), Eason et al. (1992), and Abdul-Aziz et al. (1995) found that mass flow velocities of ~100–300 km s^{-1} would be required to produce the observed Balmer line widths. In both our F10 and F11 models, chromospheric velocities are much less than these (Hγ has a maximum velocity of ~10 km s^{-1}), and we find that in these simulations the line broadening is almost entirely due to the Stark effect.

5.4. *Balmer Decrement*

The Balmer decrement represents the relative energy emitted in various Balmer lines. It is defined as the ratio of the excess flare emission in the Balmer lines relative to a fiducial, often taken to be Hβ or Hγ. Information about the electron density in the Balmer line–forming region of the atmosphere may be inferred, with steeper decrements implying smaller electron densities (García-Alvarez et al. 2002). A simple explanation for this is that as densities increase, the lower order lines become thicker, and more energy can escape in the higher order lines, making the decrement shallower. Since the decrement is a relative measure, it makes comparing flares of different sizes straightforward. In Table 1, we present Balmer decrements calculated relative to Hγ for F10 and F11 and compare them to several observations. We have also included the Ca II K decrement. For the F10 and F11 simulations we employed a six-level hydrogen atom, and therefore we could not directly calculate Balmer lines higher than Hγ in detail. To obtain line fluxes for higher order lines, we passed a "snapshot" of the atmosphere at the peak of Balmer emission to the static radiative transfer code, MULTI (Carlsson 1986). In MULTI we used a 13 level hydrogen atom, allowing us to model the Balmer lines through H12. Comparing F11 to F10 shows that

TABLE 1
BALMER DECREMENT

Source	Hβ	Hγ	Hδ	H8	H9	Ca II K
F10 flare	1.28	1.00	0.96	0.82	0.74	0.96
F11 flare	1.19	1.00	0.89	0.64	0.53	0.12
AD Leo (HP91)[a]	1.24	1.00	0.85	0.64	0.47	0.22
AD Leo (R84)[b]	...	1.00	0.85	0.53	0.39	0.15
UV Cet (P88)[c]	...	1.00	0.69	0.47	0.42	0.83
UV Cet (E92)[d]	...	1.00	0.96	0.46	0.34	0.09
YZ CMi[e]	...	1.00	0.69	0.54	0.45	...
EZ Aqr[f]	1.38	1.00	0.83	0.54	0.36	...
Solar M-class flare[g]	1.74	1.00	0.80	0.63	...	...

[a] Impulsive phase (Hawley & Pettersen 1991).
[b] Impulsive phase (Rodono et al. 1984).
[c] Flare maximum. (Phillips et al. 1988).
[d] Impulsive phase (Eason et al. 1992).
[e] Flare average (Doyle et al. 1988).
[f] Flare maximum of flare E (Jevremovic et al. 1998).
[g] Flare maximum (Johns-Krull et al. 1997).

for a larger flare, Hγ becomes relatively stronger than the other Balmer lines. All the observed Balmer decrements more closely match F11 than F10, as expected, since these flares were all relatively large. The decrements for a flare on AD Leo reported by Hawley & Pettersen (1991) are especially close to F11, indicating that the flare chromospheric structure likely resembles the structure predicted by this simulation.

5.5. *Line-to-Continuum Ratios*

The continuum carries 79% of the total emission in the F10 flare. The lines are relatively stronger in the F11 flare, with the continuum carrying only 72% of the energy. Both model predictions are considerably smaller than ratios typically observed for M dwarf flares. H03 observed a continuum emission–to–total emission ratio of ~92% for five moderate flares on AD Leo. Rodono et al. (1984) also observed a ratio of 92% for a flare on AD Leo, and for a very large flare Hawley & Pettersen (1991) obtained a ratio of 86%. Our overestimation of the relative line strength is likely due to the fact that these simulations do not reproduce the featureless ~9000 K white-light continuum observed in M dwarf flares. If we add a 9000 K blackbody spectrum to our model spectrum, we do obtain a line-to-continuum ratio of more than 90%, as expected.

Another possible reason for the significant line emission from our simulations is the shape of the beam energy spectrum. If we are overestimating the concentration of beam energy that is deposited in the upper chromosphere, the excess heating will produce too much Balmer emission. The majority of the beam energy is deposited within a relatively narrow region of the chromosphere and causes large increases in the Balmer emission. Mauas & Gomez (1997) have shown, using a Fokker-Planck description of the electron beam, that the beam energy deposition is over a wider region and higher in the atmosphere than is predicted by the analytic expression employed in these simulations. Less concentrated heating will likely produce less dramatic Balmer emission and a line-to-continuum ratio that more closely matches observations.

5.6. *UV Line Velocities*

H03 observed numerous transition region and coronal lines with the *Hubble Space Telescope* (*HST*) STIS instrument during flares on AD Leo. They found that many of the lines formed in the transition region were redshifted during the impulsive phase

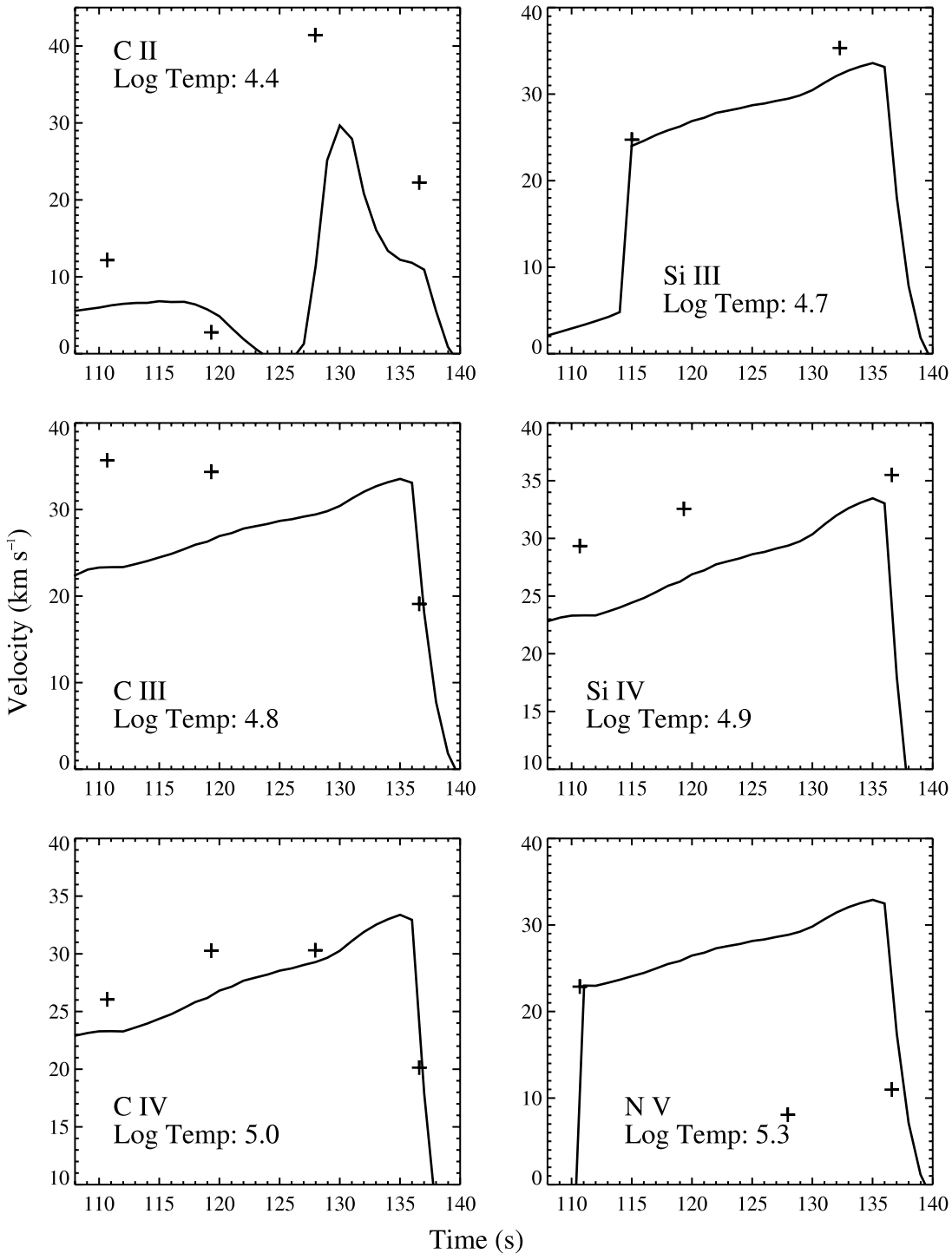

FIG. 16.—F10 plasma velocities plotted and compared to velocities obtained during flare 8 of H03. The solid lines plot velocities of the plasma at the temperature indicated, and the crosses mark the observed velocities. The labels in each panel indicate the ion measured and its formation temperature. The time axis of flare 8 has been shifted by 7.0 s.

of the flare, and they interpreted this as an example of chromospheric condensation. To compare our simulations to these observations, we used the CHIANTI (Dere et al. 1997; Young et al. 2003) database to produce synthetic line profiles for the lines observed by H03. In our flare simulations, we find multiple regions of the atmosphere with typical transition region temperatures ($\sim 10^5$). For example, at 150 s in F10 (panel 3 of Fig. 2) there are three regions with this temperature ($z = 0.5$, 3.1, and 3.6 Mm). The outer two ($z = 3.1$ and 3.6 Mm) are traveling upward, producing blueshifted emission, and the inner one ($z = 0.5$ Mm) is moving deeper into the atmosphere, causing redshifted emission. In Figure 16 we compare the velocity of the downward-directed plasma with the velocities obtained during flare 8 of H03. Both the simulation and observations exhibit velocities of 20–40 km s^{-1}, in agreement with the condensation velocities predicted by Fisher (1989).

6. CONCLUSIONS

We have constructed radiative hydrodynamic simulations of a flaring M dwarf atmosphere and used them to explore the flare-induced optical and UV emission. We find that the dynamics of the impulsive flare naturally divide into two phases, an initial gentle phase followed by a period of explosive increases in temperature and pressure. The explosive wave front creates a high-temperature bubble that expands until the wave passes through the boundary of the flux tube. The atmosphere then attains a steady state with a corona and transition region that are denser than the preflare atmosphere.

Line emission is greatly enhanced in both the moderate (F10) and strong (F11) flare simulations. As chromospheric material is evaporated into the transition region, the He II 304 line is especially enhanced, becoming the strongest line in the spectrum. Large hydrodynamic waves produced by the flare heating cause significant Doppler shifting of the line profiles. The He II 304 line exhibits a peak upward velocity of 129 km s^{-1}, and the Ca II K line has a peak downward velocity of 30 km s^{-1}. We compared the predicted velocity of our downward-directed condensation wave to velocities measured in transition region lines by H03 and found that both models and observations exhibited velocities between 20 and 40 km s^{-1}.

Stark broadening caused by the increased electron density in the flaring atmosphere makes the Balmer lines very wide. We compared our F10 Balmer profiles to the observations in H03 and found that for both observations and simulations Hβ had a width of 16 Å, and Hγ had a width of 10 Å. We also found that for the stronger Hawley & Pettersen (1991) flare, the Hγ line was similar in width and shape to the F11 Hγ line profile.

Our simulations predict elevated optical continuum emission. A large Balmer jump in the flare spectrum radiatively back-warms the atmosphere below the temperature minimum region and heats the photosphere by about 400 K for F10 and 1200 K for F11. With the elevated Paschen continuum this produces a 32% increase in the continuum level for F10 and a 129% increase for F11. The predicted photospheric temperature increase is not large enough to explain the observed blackbody continuum of $\sim$9000 K. Our predicted spectrum, when convolved with the *UBVR* filters, does produce a spectrum that looks like a 9000 K blackbody, but this depends on the presence of a large Balmer jump, which has not been seen in M dwarf flares. The optical continuum exhibits an initial dimming, which also has been observed in M dwarf flares. In our simulations, the dimming is a result of nonthermal ionizations due to the electron beam causing an overdensity of excited states of hydrogen.

We have successfully modeled velocities, line broadening, and Balmer decrements. While broadband colors are matched by our spectrum convolved with filter curves, the continuum does not match in details, predicting a large Balmer jump and a noticeable Paschen jump, which are not observed. The formation of the strong, featureless white-light continuum during stellar flares, therefore, remains a mystery.

Although we have taken great care to make these simulations as accurate as possible, we have found it necessary to make several limiting assumptions. The atmosphere is assumed to be one-dimensional, plane-parallel, and aligned with the magnetic field. This neglects the possibility that radiation can escape through the sides of the flux tube. The ion and electron temperatures are assumed to be the same. We have also assumed complete redistribution holds for all transitions. By neglecting magnetohydrodynamic (MHD) effects we have implicitly assumed that that magnetic pressure is much higher than the gas pressure and effectively confines the plasma to the flux tube.

We plan to make several improvements to these models. As mentioned above, the analytic treatment of Emslie (1978) results in the beam energy being deposited in a relatively narrow region of the atmosphere, causing steep electron density gradients and much stronger than observed Balmer emission. We plan to incorporate a model of the electron beam using Fokker-Planck kinetic theory. Preliminary analysis shows a wider range of energy deposition with a larger portion of the beam deposited in higher regions of the atmosphere than predicted by Emslie (1978). This will also provide more direct heating to the corona. With these changes, we hope to be able to model a larger flare loop, as is probably more appropriate for the stellar flare case. This may allow the stellar flare explosive wave to pass through the top of the loop and thereby allow the flare loop to obtain a steady state as in the solar case.

This work has been partially funded by NSF grant AST 02-05875 and *HST* grants AR-10312 and GO-8613. The computations presented here were carried out on the Astronomy Condor Network at the University of Washington, and we would especially like to thank John Bochanski for contributing many hours of computer time.

REFERENCES

Abbett, W. P., & Hawley, S. L. 1999, ApJ, 521, 906 (AH99)
Abdul-Aziz, H., et al. 1995, A&AS, 114, 509
Alekseev, I. Y., et al. 1994, A&A, 288, 502
Allred, J. C., Hawley, S. L., Abbett, W. P., & Carlsson, M. 2005, ApJ, 630, 573
Cargill, P. J. 1994, ApJ, 422, 381
Carlsson, M. 1986, A Computer Program for Solving Multi-Level Non-LTE Problems in Moving or Static Atmospheres (Uppsala: Uppsala Astron. Rep. 33)
Carlsson, M., & Stein, R. F. 1994, in Chromospheric Dynamics, Proc. of Miniworkshop, ed. M. Carlsson (Oslo: Univ. Oslo, Inst. Theor. Astrophys.), 47
———. 1995, ApJ, 440, L29
———. 1997, ApJ, 481, 500
Cristaldi, S., Rodono, M., & Gershberg, R. E. 1980, A&A, 89, 123
Dere, K. P., Landi, E., Mason, H. E., Monsignori Fossi, B. C., & Young, P. R. 1997, A&AS, 125, 149
Doyle, J. G., Butler, C. J., Bryne, P. B., & van den Oord, G. H. J. 1988, A&A, 193, 229
Eason, E. L. E., Giampapa, M. S., Radick, R. R., Worden, S. P., & Hege, E. K. 1992, AJ, 104, 1161
Emslie, A. G. 1978, ApJ, 224, 241
Fisher, G. H. 1989, ApJ, 346, 1019
García-Alvarez, D., Jevremović, D., Doyle, J. G., & Butler, C. J. 2002, A&A, 383, 548
Giampapa, M. S., Africano, J. L., Klimke, A., Parks, J., Quigley, R. J., Robinson, R. D., & Worden, S. P. 1982, ApJ, 252, L39
Guedel, M., Benz, A. O., Schmitt, J. H. M. M., & Skinner, S. L. 1996, ApJ, 471, 1002
Gustafsson, B. 1973, A FORTRAN Program for Calculating "Continuous" Absorption Coefficients of Stellar Atmospheres (Uppsala: Landstingets)
Haisch, B., Strong, K. T., & Rodono, M. 1991, ARA&A, 29, 275
Hawley, S. L., & Fisher, G. H. 1992, ApJS, 78, 565
Hawley, S. L., & Pettersen, B. R. 1991, ApJ, 378, 725
Hawley, S. L., et al. 1995, ApJ, 453, 464
———. 2003, ApJ, 597, 535 (H03)
Holman, G. D., Sui, L., Schwartz, R. A., & Emslie, A. G. 2003, ApJ, 595, L97
Hudson, H. S., Acton, L. W., Hirayama, T., & Uchida, Y. 1992, PASJ, 44, L77
Jevremovic, D., Butler, C. J., Drake, S. A., O'Donoghue, D., & van Wyk, F. 1998, A&A, 338, 1057
Johns-Krull, C. M., Hawley, S. L., Basri, G., & Valenti, J. A. 1997, ApJS, 112, 221
Johns-Krull, C. M., & Valenti, J. A. 1996, ApJ, 459, L95

Mauas, P. J. D., & Gomez, D. O. 1997, ApJ, 483, 496
McTiernan, J. M., Fisher, G. H., & Li, P. 1999, ApJ, 514, 472
Mitra-Kraev, U., et al. 2005, A&A, 431, 679
Neupert, W. M. 1968, ApJ, 153, L59
Phillips, K. J. H., Bromage, G. E., Dufton, P. L., Keenan, F. P., & Kingston, A. E. 1988, MNRAS, 235, 573
Rodono, M., et al. 1984, in Fourth European *IUE* Conf. (SP-218; Noordwijk: ESA), 247
Scharmer, G. B., & Carlsson, M. 1985, J. Comput. Phys., 59, 56
Smith, R. K., Brickhouse, N. S., Liedahl, D. A., & Raymond, J. C. 2001, ApJ, 556, L91
Young, P. R., Del Zanna, G., Landi, E., Dere, K. P., Mason, H. E., & Landini, M. 2003, ApJS, 144, 135